



Cite this: *J. Mater. Chem. C*, 2019, 7, 4838

Unprecedented 30 K hysteresis across switchable dielectric and magnetic properties in a bright luminescent organic–inorganic halide $(\text{CH}_6\text{N}_3)_2\text{MnCl}_4^\dagger$

Abhijit Sen,^a Diptikanta Swain,^b Tayur N. Guru Row ^b and A. Sundaresan ^{*a}

Multifunctional materials that exhibit various switchable properties and simultaneously feature excellent luminescent properties boast tremendous technological importance. However, realization of such materials is still elusive, as integration of these independent yet technologically important properties in single materials is fairly challenging. Here, we report a new highly photoluminescent hybrid $(\text{CH}_6\text{N}_3)_2\text{MnCl}_4$ ($\text{CH}_6\text{N}_3 =$ guanidinium cation, GC) that exhibits an unprecedented 30 K wide hysteresis in dielectric and magnetic switching across the structural phase transition (SPT). The compound uniquely features trimeric $(\text{Mn}_3\text{Cl}_{12})^{6-}$ units composed of face-sharing MnCl_6 octahedra in its zero-dimensional crystal structure and undergoes a thermally induced reversible structural transition at 166/195 K. The high and low dielectric states show a remarkable 30 K wide reversible dielectric switching which is mainly portrayed by the relative population of quadrupolar and dipolar moments of disordered and ordered phases of GCs. Only a small change in the crystal volume across the transition is reflected in subtle magnetic switching. Moreover, the material exhibits an intense orange–red emission under ultraviolet excitation at room temperature with long lifetime (1.71 ms) and large quantum yield (39.5%). This report suggests a promising strategy to construct truly multifunctional optoelectronic materials and may be helpful to improve the understanding and control of switchable physical properties and luminescence in supramolecular materials.

Received 2nd February 2019,
Accepted 27th March 2019

DOI: 10.1039/c9tc00663j

rsc.li/materials-c

Introduction

The spectrum of multifunctional materials showing one or more stimuli-responsive switchable properties exhibit compelling richness in terms of understanding and application potential and thus has continuously brought impetus to modern-day materials research.^{1–4} In principle, the switching behaviour of bulk physical/chemical properties among two (or more) distinct states can be tuned by certain external stimuli (light, heat, magnetic field, electrical bias or pressure) which can find possible applications as sensors, displays, storage and memory devices.^{5–7} Among these various stimuli, temperature is most frequently used as it can be controlled very efficiently. Thus recent years have seen a surge in reports of thermally driven switchable materials from both academic and application perspectives.^{8–11} Considering various

switchable properties, magnetization and dielectrics are technologically most important. In switchable magnetization, cumulative magnetic interaction among different sites changes due to the rearrangement of spins between high and low spin states (known as “spin crossover”).^{12,13} Meanwhile, switchable dielectrics deal with redistribution of polar components, leading to the appearance of high and low dielectric states (HDS and LDS, respectively).^{14,15}

Fundamentally, the dielectric property of a material represents collective behaviour of polarizable bound charges (polar components) where the degree of polarizability is described by the real part ϵ_r of the complex dielectric constant ($\epsilon = \epsilon_r - i\epsilon_i$). In switchable dielectrics, the switching feature arises mainly due to the dynamic/motional changes in polar components (molecules or ions) between “disordered” (liquid) and “ordered” (frozen) states across the transition.^{14,15} In molecular dielectrics, the switching behaviour often manifests as a structural phase transition (SPT) as the reorientation and/or ordering of the dynamic components across temperature often instigate symmetry breaking. Up to now, dielectric switching has been realized mainly in inclusion compounds and MOFs owing to their structural diversity and various supramolecular interactions present among components. As examples, Wang *et al.* have reported azido-bridged perovskite-type compounds $[(\text{CH}_3)_n\text{NH}_{4-n}][\text{Mn}(\text{N}_3)_3]$ ($n = 1–4$), which combine

^a School of Advanced Materials and Chemistry and Physics of Materials Unit, Jawaharlal Nehru Centre for Advanced Scientific Research, Jakkur, Bangalore 560 064, India. E-mail: sundaresan@jncasr.ac.in

^b Solid State and Structural Chemistry Unit, Indian Institute of Science, Bangalore 560 012, India

[†] Electronic supplementary information (ESI) available. CCDC 1891611 and 1891612. For ESI and crystallographic data in CIF or other electronic format see DOI: 10.1039/c9tc00663j

both dielectric and magnetic bistabilities at the SPT.¹⁶ Very recently, an inclusion compound $(\text{C}_2\text{H}_6\text{N}_3)^+(\text{H}_2\text{PO}_4)^-$ has been reported to exhibit 40 K wide thermal hysteresis near room temperature across the SPT which is triggered by cationic rotation and adjustment in crystal packing.¹⁷ In this context, organic-inorganic halides (OIHs) appear highly suited, as their crystal structures can efficiently combine rigid metal halide architectures and dynamic ammonium cations in various fashions.¹⁸ OIHs are well-known to exhibit diverse crystal structures, undergo thermally induced SPTs and combine multiple physical properties in a single phase.^{19–26} Among OIHs, low-dimensional crystals offer ample free space for the ammonium cations, which is beneficial for the dynamic behaviour and thus dielectric switching behaviour to flourish. Thus, low-dimensional OIHs with appropriate metal ions can form a rare and technologically important class of materials that integrate multiple switchable properties across the SPT and also exhibit intriguing physical properties. For example, Luo *et al.* reported the zero-dimensional compound $[\text{C}_6\text{H}_{14}\text{N}][\text{FeBr}_4]$ to combine both dielectric and magnetic anomalies at the SPT.¹⁰ Recently, the red photoluminescent compound (2-methylimidazolium) $\text{MnCl}_3(\text{H}_2\text{O})$ has been reported to display both dielectric and optical switching properties across the order–disorder SPT.²⁷ Among other Mn-based hybrids, Ren-Gen Xiong *et al.* have recently reported BaNiO_3 -like hexagonal perovskite structures in the compounds $\text{TMBMMnBr}_3(\text{Me}_3\text{NCH}_2\text{BrMnBr}_3)$ and $\text{TMCMMnCl}_3(\text{Me}_3\text{NCH}_2\text{ClMnCl}_3)$, both of which exhibit dielectric switching associated with structural phase transitions at high temperature and also very large piezoelectric coefficients.^{28,29}

The transition temperature (T_c) and thermal hysteresis (ΔT) are the two major attributes of thermally switchable dielectrics. Among these, T_c mainly depends on the crystalline packing and effective size of the rotating component(s) while ΔT is mostly affected by the degree of cooperativity among different microscopic interactions across the transition.^{17,30} In reality, design of switchable molecular OIHs that assemble static and dynamic components and give rise to high T_c and sizeable ΔT values is fairly challenging. This is due to insufficient knowledge on the complicated mechanism of orientational changes in dynamic components across T_c . Up to now, only a handful of thermally switchable OIHs are reported where the ΔT and T_c have been controlled *via* modulation of “weak” H-bonding and short contact bonding present in the materials. Increasing the number of these supramolecular interactions can fundamentally stabilize the structure to a greater extent and increase ΔT of the SPT.

Here, with conscious selection of planar guanidinium cations (GCs) $(\text{CH}_6\text{N}_3)^+$, we report a new luminescent OIH $(\text{CH}_6\text{N}_3)_2\text{MnCl}_4$ (**1**) that exhibits multiple switchable properties at the SPT. The compound notably contains unique trimeric $(\text{Mn}_3\text{Cl}_{12})^{6-}$ units and ion-pair interactions among GCs in the zero-dimensional crystal structure. Thermally driven reversible SPT is observed at 166/195 K (cooling/heating), exhibiting an intriguingly large 30 K hysteresis. Remarkably, the transition is seen to be accompanied by switchable dielectric and magnetic anomalies. Dynamic (dipolar) and frozen (quadrupolar) phases of GCs are mainly responsible for the dielectric switching while subtle changes in crystal packing and volume indicates the appearance of magnetic switching.

The presence of octahedral Mn^{2+} imparts brilliant photoluminescence features under UV radiation at room temperature.

Experimental section

Synthesis

0.42 g (4.4 mmol) of guanidine hydrochloride ($\text{CH}_6\text{N}_3\text{Cl}$) and 0.436 g (2.2 mmol) of manganese chloride tetrahydrate ($\text{MnCl}_2 \cdot 4\text{H}_2\text{O}$) were thoroughly dissolved in deionized water followed by slow evaporation at 300 K. Light pink rod shaped crystals formed after about three weeks. The elemental analyses were carried out using a Thermo Scientific Flash 2000 CHN analyzer.

Thermal measurements

Thermogravimetric analysis (TGA) data was recorded using a Mettler Toledo TGA 850 under a nitrogen atmosphere from 298 to 1073 K with a ramp rate of 5 K min^{-1} .

Modulated DSC data were recorded using a TA Q2000 instrument. 8 mg of crushed crystals were added to an aluminium crucible and data were collected in the temperature range of 93–463 K under a nitrogen atmosphere. The heating and cooling rate was kept at 2 K min^{-1} . The single crystals were pre-dried under vacuum for 12 h and then crushed for these experiments.

Temperature dependent heat capacity (HC) was recorded in the temperature range of 130–220 K using a Quantum Design PPMS. For this experiment, first the HC of addenda (which includes Apeizon grease and the sample platform, and define the thermodynamic surrounding) was recorded, following which a suitable crystal piece was mounted on the same grease and the heat capacity of the whole setup (system + surrounding) was recorded. HC was measured *via* the relaxation technique where HC of addenda was auto-subtracted to derive the HC of the compound.

Single-crystal data collection

For single-crystal data collection, a suitable crystal piece was mounted inside a Lindemann capillary which was then mounted on top of the goniometer head. Variable-temperature single-crystal X-ray diffraction data were collected on an Oxford Xcalibur (Mova) diffractometer equipped with an EOS CCD detector and a microfocus sealed tube using $\text{Mo-K}\alpha$ radiation ($\lambda = 0.71073 \text{ \AA}$). Data collection at low temperature was performed using an Oxford Cobra open stream non-liquid nitrogen cooling device. Refinement of cell parameters, data integration and reduction were accomplished by using the program CrysAlisPro.³¹ The structure solution was obtained from SHELXS^{32,33} and refined by using SHELXS 2018 included in the WinGX suite.³⁴

UV-Vis absorption and photoluminescence studies

Diffuse reflectance spectra of crushed crystals were recorded using a Perkin–Elmer Lambda 900 spectrometer. Background correction was performed by subtracting pre-recorded reflectance spectra of a BaSO_4 disc from the compound spectra. Further, the background corrected data was converted into absorbance equivalents by using the Kubelka–Munk function. PL and PLE spectra were collected using a 450 W xenon lamp source on an FLSP920 spectrometer (Edinburgh Instruments). Lifetime measurements

were carried out on an EPL-405 ps pulsed diode laser used as the excitation source ($\lambda_{\text{ex}} = 365 \text{ nm}$). The absolute PL QY was determined using an integrating sphere.

Dielectric measurements

Structural transition features were visualized *via* studying the temperature and frequency dependence of the dielectric constant. Electrical contacts were put on both end surfaces of a rod-shaped single crystal using commercial silver paste. The sample was connected to a multiprobe and inserted inside a Quantum Design PPMS chamber. Capacitance and loss were measured using an Agilent (E4980A) Precision LCR meter in the temperature range of 150–220 K with 2 K min^{-1} heating/cooling rate in the frequency range of 5–300 kHz under an applied trigger voltage of 0.5 V.

Magnetic measurements

DC magnetic susceptibility and magnetization measurements on single crystals were carried out using a Quantum Design SQUID-based MPMSXL-3-type magnetometer. Zero-field cooled and field cooled data were recorded in the temperature range of 1.8–350 K with an applied magnetic field of 100 Oe. To observe structural transition features, data were recorded during both cooling and warming under an applied field of 100 Oe. Isothermal magnetizations were measured at 1.8 and 300 K with a field sweep range of $\pm 7 \text{ T}$.

Results and discussion

Structural studies

Compound **1** was obtained as pale pink rod shaped crystals *via* slowly evaporating an aqueous solution of guanidine hydrochloride and manganese chloride tetrahydrate. The chemical composition and purity of the as-grown crystals were confirmed

by elemental analysis which yielded the following mass percentages (calculated values in parentheses): H, 3.76 (3.81); C, 7.54 (7.57); N, 26.55 (26.51); Cl, 44.76 (44.74%).

The structure of **1** at 295 K, as determined from single-crystal X-ray diffraction is monoclinic, space group $P2_1/c$ with $a = 8.6611(4)$, $b = 27.0793(14)$, $c = 15.6284(7) \text{ \AA}$, $\beta = 93.237(4)^\circ$ and $Z = 12$ (refinement parameters and important structural details are included in ESI,† Tables S1 and S2). The asymmetric unit contains three formula units of $(\text{CH}_6\text{N}_3)_2\text{MnCl}_4$ where all atoms occupy general crystallographic positions (Wyckoff: 4e) (Fig. 1(a)). Importantly, two out of the six crystallographically independent GCs are significantly disordered at room temperature (Fig. 1(a)). Very importantly, each of the three crystallographically independent Mn atoms in the asymmetric unit are each coordinated with six Cl atoms, forming MnCl_6 octahedral units. Further, these MnCl_6 units share faces with each other resulting a trimeric $(\text{Mn}_3\text{Cl}_{12})^{6-}$ unit (Mn–Mn distances of 3.3168(12) and 3.3380(12) \AA) as can be seen in Fig. 1(a). This type of trimeric unit is unprecedented in OIH crystals and is intermediate between infinite one dimensional chain of MnCl_6 octahedra and single MnCl_6 units. As expected, the MnCl_6 octahedra are distorted with Mn–Cl bond distances and Cl–Mn–Cl angles in the range of 2.4605(16)–2.6990(16) \AA and $165.27(5)$ – $179.74(6)^\circ$, respectively (Fig. 1(a)). Notably, the two end MnCl_6 members in the $(\text{Mn}_3\text{Cl}_{12})^{6-}$ unit are more distorted compared to the central MnCl_6 octahedron. The distortions are quantified by analyzing Cl–Mn–Cl angles of each octahedral unit where the two end members have angles $165.27(5)$, $168.21(7)$, $172.84(7)^\circ$ and $170.34(6)$, $170.81(5)$, $170.86(7)^\circ$, whereas the angles for the central octahedral unit are $177.90(6)$, $178.29(6)$, $179.74(6)^\circ$. Similarly, the Mn–Cl bond distances for the two end octahedra are more varied (2.4605(16)–2.6725(15) \AA and 2.4614(17)–2.6990(16) \AA) compared to the central one (2.5059(13)–2.5663(16) \AA) (Fig. 1(c)). Further the inter-octahedral angles Mn–Cl–Mn, which indicate the octahedral rotation, are in the range $78.11(4)$ – $80.79(4)^\circ$.

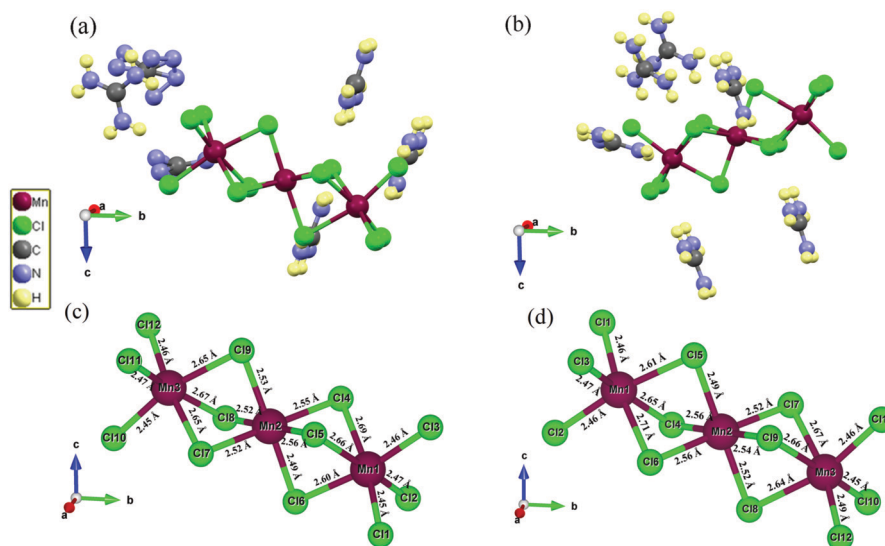


Fig. 1 Molecular structures of compound **1** at different temperatures: (a) asymmetric unit at 295 K, two guanidinium cations are thermally disordered, (b) asymmetric unit at 150 K, all the guanidinium ions are in a thermally ordered state. The trimeric $(\text{Mn}_3\text{Cl}_{12})^{6-}$ units at (c) 295 K and at (d) 150 K, the Mn–Cl bond distances have been included.

To see the effect of temperature on disorder, we recorded low-temperature single-crystal X-ray data. On cooling to 150 K, the crystal symmetry changes into the orthorhombic crystal system, space group $P2_12_12_1$ with $a = 8.6227(5)$, $b = 27.0625(12)$, $c = 15.4503(7)$ Å and $Z = 12$. Although the lattice parameters do not change substantially as compared to the 295 K structure, completely ordered GCs are observed at the lower temperature (Fig. 1(b)). In the asymmetric unit, each of three formula units of $(\text{CH}_6\text{N}_3)_2\text{MnCl}_4$ occupy general crystallographic positions (Wyckoff: 4a). In the $(\text{Mn}_3\text{Cl}_{12})^{6-}$ unit, increased distortions in MnCl_6 octahedra compared to the room-temperature structure are observed. The Cl–Mn–Cl angles for the MnCl_6 octahedra are in the range of $168.99(13)$ – $171.27(13)$, $177.28(14)$ – $179.64(14)$ and $164.27(12)$ – $172.24(13)^\circ$ while the Mn–Cl bond distances are in the range of $2.464(3)$ – $2.711(4)$, $2.494(4)$ – $2.567(4)$ and $2.452(4)$ – $2.674(4)$ Å (see Fig. 1(d)). Similarly, the inter-octahedral angles are in the range $77.85(11)$ – $80.88(9)$ and $80.07(10)$ – $80.50(9)^\circ$.

At 295 K, seven H-bonding interactions are observed between each $(\text{Mn}_3\text{Cl}_{12})^{6-}$ unit and GCs, which on cooling, increases to nine at 150 K (Fig. 2(a) and (b)). Considering the non-spherical charge distribution around planar GCs (D_{3h} symmetry in planar form), a substantial quadrupole moment is expected. This moment, along with cavitation effects and van der Waals interactions, often influences supramolecular ion-pair interactions between GCs, as have been theoretically and experimentally well-observed in aqueous solution and in biomolecules.^{35–37} To our excitement, the C–C distances between nearest and next nearest neighbor GCs in both phases of **1** (3.948 – $5.475(8)$ Å at 295 K and $3.947(19)$ – $5.452(12)$ Å at 150 K, only eclipsed arrangements are considered) are in excellent agreement with the optimum range of C–C distance for facile ion-pair interactions. Thus, considerable ion-pair interactions among thermally ordered GCs are expected to be present, further stabilizing the structure in both phases of **1** (Fig. 2(c)). Such extensive supramolecular interactions among the GCs along different directions possibly obstruct linear extension of the Mn–Cl architecture thereby resulting in an overall zero-dimensional structure.

Structural phase transition

DSC and specific heat measurements are reliable and widely used methods to study thermally induced SPTs. In view of the structural change with temperature, DSC and heat capacity measurements were carried out. As shown in Fig. 3(a), the DSC curve shows endothermic/exothermic anomalies at 166/195 K (cooling/heating) indicating a reversible transition. Sharp anomalies with a very large thermal hysteresis of 30 K indicates the first-order nature of the transition. Such large hysteresis across SPTs are seldom observed among OIH crystals. We believe that the extensive supramolecular interactions present among the GCs and $(\text{Mn}_3\text{Cl}_{12})^{6-}$ units hinder the structural transition process, thereby increasing the thermal hysteresis. Of relevance, very recently a 30 K wide hysteresis has been observed across the SPT in an ionic compound $[\text{C}_2\text{H}_6\text{N}_5]_2[(\text{H}_2\text{O})_2\text{SO}_4]$ where large hysteresis arises, as the presence of hydrogen bonds hinder the rotation of ionic components within the compact crystal structure.³⁸ In the present system, the anomaly during cooling is broader than the heating anomaly, with calculated enthalpy changes being 11.09 and 17.57 J mol^{−1} for cooling and heating, respectively (Fig. S5, ESI†). This difference rather indicates that ordering and orientational changes during cooling are comparatively sluggish. Specifically, for heat data recorded during warming, a sharp anomaly is observed at 195 K (Fig. 3(b)) and the corresponding entropy change across the transition is 0.34 J mol^{−1} K^{−1} as has been estimated from C_p/T data. The calculated value of N is 1.04 from the Boltzmann equation $\Delta S = R \ln N$; (R : gas constant and N : ratio of distinguishable configurations) which indicates the order–disorder nature of the phase transition.

Switchable dielectric properties

Typically the macroscopic dielectric properties of a material show distinct features across the STP due to change in dipolar orientations. The temperature dependence of the complex dielectric permittivity has been probed during both cooling and heating

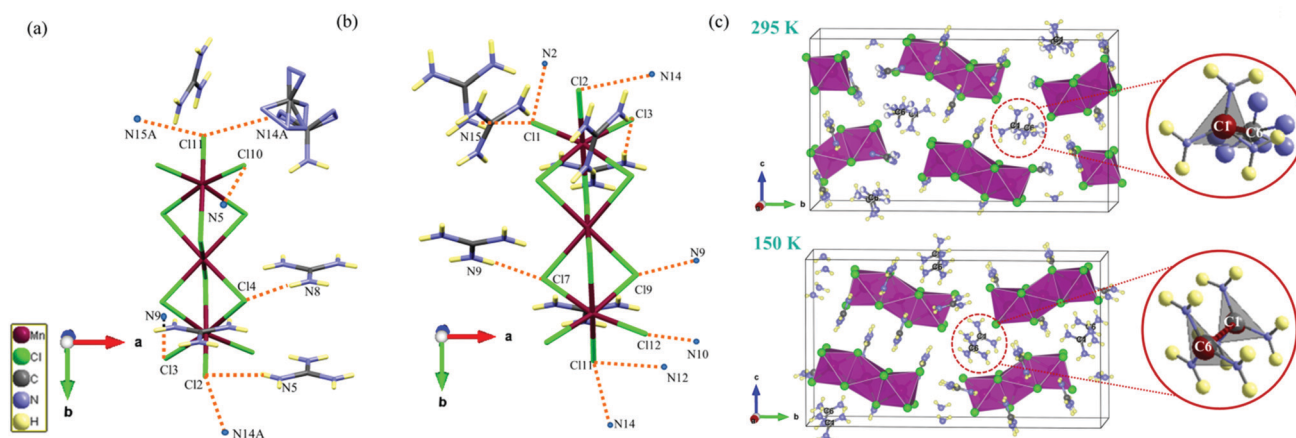


Fig. 2 Views of various supramolecular interactions present among different components in the crystals. Molecular units at (a) 295 K and (b) 150 K showing hydrogen-bonding interactions present between each $(\text{Mn}_3\text{Cl}_{12})^{6-}$ unit and GCs. (c) Unit cell diagrams of **1** at 295 and 150 K; zoomed fractions show modulation of one of many ion-pair interactions among GCs across the SPT.

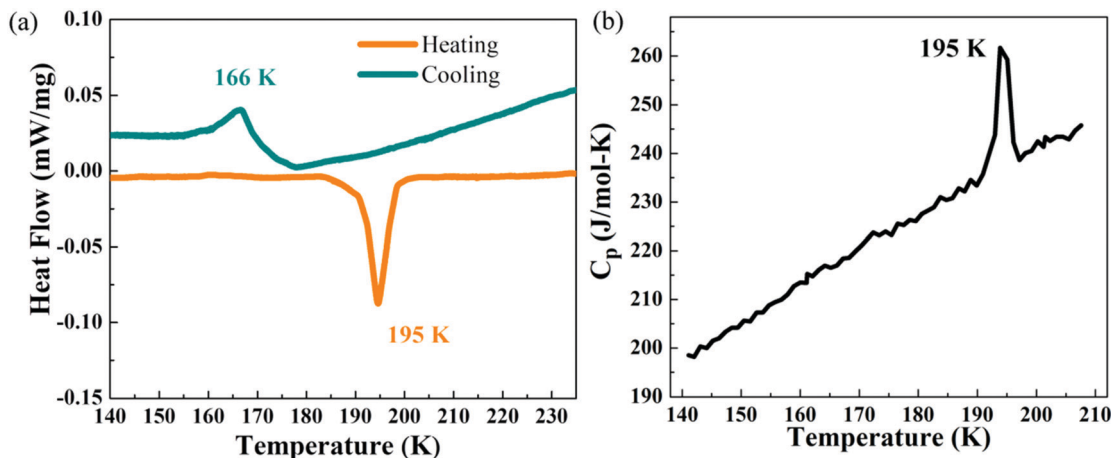


Fig. 3 Structural transition features: (a) reversible DSC anomalies, (b) heat capacity data obtained during the heating procedure.

in the temperature range of 220–120 K at different frequencies between 5 and 300 kHz.

In view of the rod shape of the crystals, measurements were carried out along the crystallographic *b*-axis. When measured under 50 kHz frequency, the real part of dielectric constant, ϵ_r , gradually decreases during cooling and reaches a value of 29.5 at 166 K (HDS). At 166 K, it undergoes a distinct step-like decrease to a value of 27 (LDS) (Fig. 4(a)) after which it decreases very slowly. During heating, the anomaly is seen to appear at 195 K confirming the reversible nature. The transition is a direct manifestation of the aforementioned SPT where the large thermal hysteresis of 30 K supports the first-order nature. From the crystal structure analysis, thermally disordered and ordered phases of GCs are observed at above the SPT while below the SPT all GCs are in the thermally ordered state. The GCs are also seen to reorient across the SPT. Additionally, cooperative displacements in $(\text{Mn}_3\text{Cl}_{12})^{6-}$ units across the transition are observed. Here, it is worth mentioning that the GCs in the thermally ordered state (LDS) are planar molecules that possess almost no dipole moment but do have some quadrupole moment resulting from non-spherical charge distribution.^{39,40} Thermal disorder in GCs destroys the planar structure and as a result the dipole moment increases. Thus, the observed

high dielectric state has significant contributions from relative populations of quadrupolar and dipolar GCs above the STP. The reorientation of GCs and displacements in $(\text{Mn}_3\text{Cl}_{12})^{6-}$ units also contribute to the overall polarity change. These collectively induce changes in overall polarity and give rise to HDS and LDS, respectively. Almost no frequency dispersion of dielectric constant and also no lossy behaviour have been observed in the dielectric data (Fig. 4(b) and (c)), which indicates that dipolar changes are fast across T_c . Overall, such distinct switchable transitions associated with large hysteresis, suggests that the material can be used as a switchable dielectric material, and also an increase in number of supramolecular interactions can effectively increase the thermal hysteresis across dielectric switching.

Magnetic properties

Considering the unique $(\text{Mn}_3\text{Cl}_{12})^{6-}$ units in the crystal, the magnetization behaviour of **1** is of interest. The temperature dependent inverse dc susceptibility (100 Oe, field cooled) reveals paramagnetic behaviour with no magnetic ordering down to 1.8 K (Fig. 5(a)). For inverse magnetic susceptibility (χ^{-1}) vs. *T* data, a weak anomaly was observed at 195 K (Fig. 5(a) inset) which agrees nicely with the DSC heating anomaly.

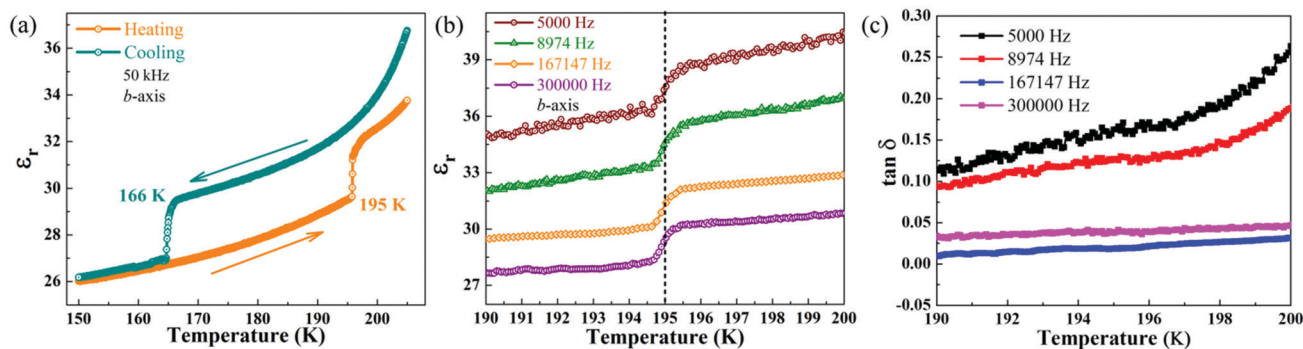


Fig. 4 Thermally switchable dielectric properties of **1**: (a) temperature dependence of the real part of complex dielectric constant recorded at 50 kHz, (b) dielectric constant under different frequencies showing the intrinsic nature of the transition, (c) temperature-dependent dielectric loss ($\tan \delta$) at different frequencies.

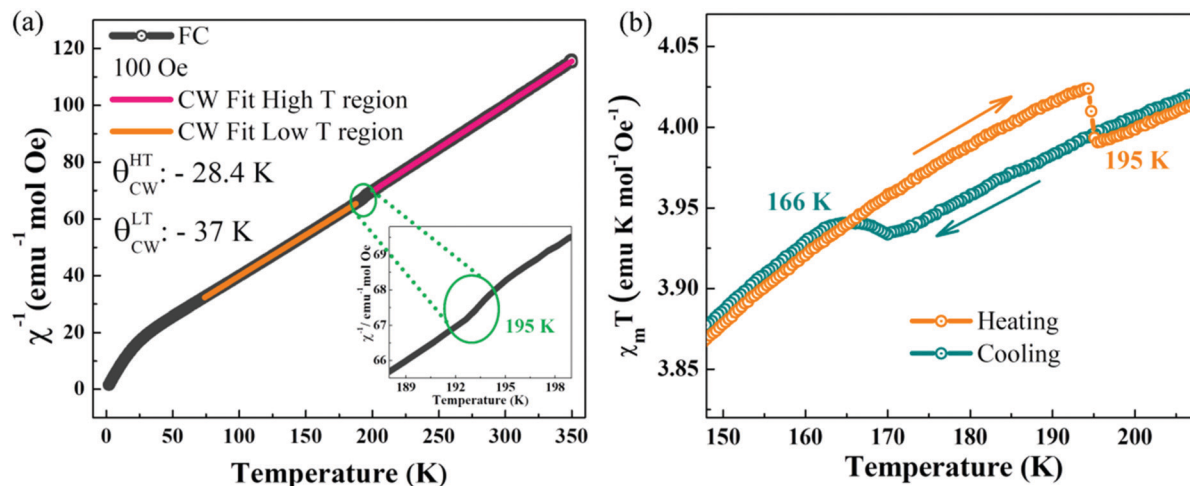


Fig. 5 (a) Temperature-dependent inverse magnetic susceptibility of **1** under a 100 Oe dc field with Curie–Weiss fitting parameters included. (b) Reversible magnetic switching observed at the SPT under a 1000 Oe dc field recorded during cooling and heating.

This indicates that the anomaly can be a direct manifestation of the SPT. To confirm this, dc susceptibility vs. temperature data were recorded during both heating and cooling. Remarkably, temperature dependent $\chi_m T$ exhibits switching behaviour with 30 K wide thermal hysteresis (Fig. 5(b)). During cooling, $\chi_m T$ gradually decreases and reaches a value of $3.9356 \text{ emu K mol}^{-1} \text{ Oe}^{-1}$ at 168 K below which it distinctly increases to $3.9382 \text{ emu K mol}^{-1} \text{ Oe}^{-1}$ in a step-like fashion. During heating, a similar step-like anomaly appeared at 195 K, where $\chi_m T$ decreases from 4.02 to $3.99 \text{ emu K mol}^{-1} \text{ Oe}^{-1}$. Such excellent agreement of magnetic switching with DSC results implies that the switching process is well coupled with the SPT. The very small switching magnitude rules out the possibility of a spin state transition. Across the SPT, minute changes are observed in Mn–Mn distances and Cl–Mn–Cl angles within $(\text{Mn}_3\text{Cl}_{12})^{6-}$ trimers. The relative distances among trimers along different directions in the crystal structure also vary across the SPT. Such structural changes across the SPT induce changes in magnetic coupling and thus reversible, subtle magnetic switching is observed.

Photoluminescence properties

In addition to the switching behaviours, the as-grown crystals exhibit fascinating photoluminescence properties. The pale pink crystals are transparent under ambient light (Fig. 6(a) top) while under UV spectrum, they show bright reddish luminescence (Fig. 6(a) bottom). This indicates that the luminescence stems from the bulk material. The UV-Vis absorbance spectra (Fig. 6(b), grey) is typical of electronic transitions between the ground and different excited states of Mn^{2+} ion in an octahedral ligand field.^{41–44} Specifically, the broad absorption at 533 nm is produced by the $(t_{2g})^3(e_g)^2 \rightarrow (t_{2g})^4(e_g)^1$ electronic transition in octahedral Mn^{2+} ions.^{41,45} In the emission spectrum ($\lambda_{\text{ex}} = 365 \text{ nm}$), a strong maximum centred at 645 nm (fwhm $\sim 90 \text{ nm}$) is observed (Fig. 6(b), pink). To find the contributions to this luminescence, we have recorded the PL excitation (PLE) spectrum. Interestingly, the PLE spectra (Fig. 6(b), olive) matches well with the absorption spectra, suggesting that almost all the absorption bands contribute towards the observed emission.²⁷ The emission is seen to be associated with a single decay process with a long lifetime of

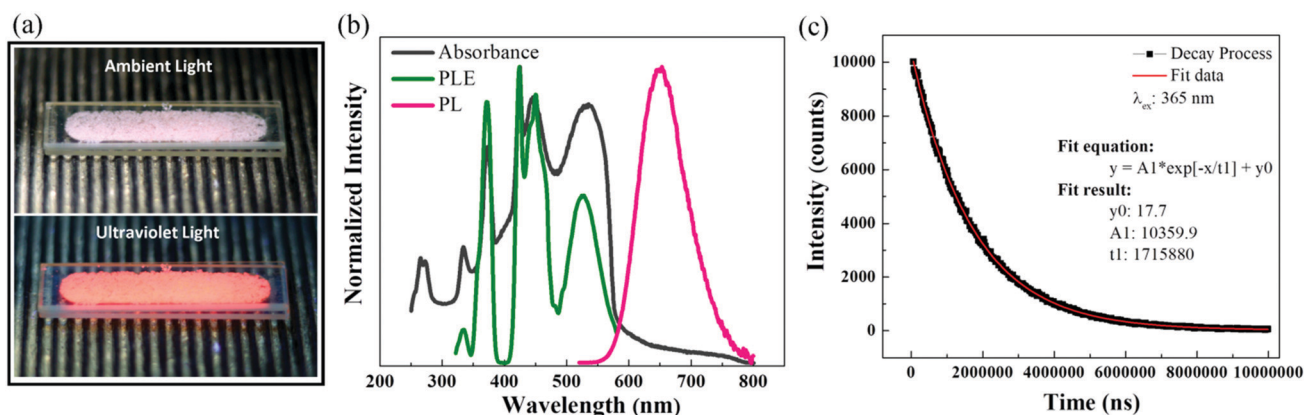


Fig. 6 Photoluminescence properties: crushed crystals under (a) top ambient light and bottom UV light (365 nm), (b) UV-Vis absorbance (grey), PLE (olive) and PL (pink) spectra and (c) photoluminescence decay lifetime analysis showing single exponential decay behaviour.

Table 1 Literature comparisons of luminescence

Compound	Lifetime	Quantum yield (%)	Ref.
(C ₄ H ₈ N)MnCl ₃	515 μs	56	44
(C ₄ H ₁₀ N)MnCl ₃	333.6 μs	28.2	45
(CH ₆ N ₃) ₂ MnCl ₄	1.71 ms	39.5	This work

1.71 ms and absolute quantum yield (QY) value of 39.5% (Fig. 6(c)). The experimental QY value lies in between that of two well-known highly luminescent linear chain hybrids (pyrrolidinium)MnCl₃ and (3-pyrrolinium)MnCl₃, while the estimated lifetime is highest among these (Table 1).^{44,45} We have also recorded the photoluminescence spectra across the phase transition temperature during cooling (cooling rate: 10 K min⁻¹). It is observed that with decrease in temperature, the emission maxima shifts to longer wavelengths and also the emission intensity gets enhanced gradually (Fig. S5(a), ESI[†]). Most interestingly, a step-like increase in intensity was observed at 160 K on cooling (Fig. S5(b), ESI[†]). Such a distinct change indicates that the material may have potential to be used as an optical switch.

Given its brilliant emission characteristics, the material strongly promises applicability in optical coatings and semiconductor devices.

Conclusions

We have successfully synthesized a new highly luminescent hybrid (CH₆N₃)₂MnCl₄ that exhibits unprecedented 30 K wide hysteresis in thermally induced dielectric and magnetic switching, accompanying a structural phase transition. The compound exhibits unique (Mn₃Cl₁₂)⁶⁻ units and ion-pair interactions in its zero-dimensional structure. The large hysteresis mainly arises from the complicated modulation of extensive supramolecular interactions across *T_c*. The high and low dielectric states across switching anomalies are mainly governed by the population of disordered and frozen phases of GCs. Changes in crystal volume and packing in the vicinity of *T_c* give rise to reversible, weak magnetic anomalies. The presence of octahedral Mn²⁺ ions leads to a fascinating bright orange-red emission at 645 nm under ultraviolet excitation with long lifetime and sizable quantum yield. Overall, this work suggests that a high number of supramolecular interactions can effectively increase the thermal hysteresis of switching, while compound **1** may have potential use in the construction of switchable dielectric and optical display devices.

Conflicts of interest

There are no conflicts to declare.

Acknowledgements

We thank International Centre for Materials Science and Sheikh Saqr Laboratory at Jawaharlal Nehru Centre for Advanced Scientific Research for providing experimental facilities. We thank

Dr Murthy Grandhi and Prof. R. Viswanatha for providing the lifetime measurement facility, Mr Ganesh, Mr Anaranya Ghorai and Prof. K. S. Narayan for helping in quantum yield and low temperature photoluminescence measurements.

Notes and references

- P. Theato, B. S. Sumerlin, R. K. O'Reilly and T. H. Epps III, *Chem. Soc. Rev.*, 2013, **42**, 7055–7056.
- P.-P. Shi, Q. Ye, Q. Li, H.-T. Wang, D.-W. Fu, Y. Zhang and R.-G. Xiong, *Chem. Mater.*, 2014, **26**, 6042–6049.
- M. A. C. Stuart, W. T. S. Huck, J. Genzer, M. Müller, C. Ober, M. Stamm, G. B. Sukhorukov, I. Szleifer, V. V. Tsukruk, M. Urban, F. Winnik, S. Zauscher, I. Luzinov and S. Minko, *Nat. Mater.*, 2010, **9**, 101.
- O. Sato, *Nat. Chem.*, 2016, **8**, 644.
- J. A. Real, A. B. Gaspar and M. C. Muñoz, *Dalton Trans.*, 2005, 2062–2079.
- O. Sato, J. Tao and Y.-Z. Zhang, *Angew. Chem., Int. Ed.*, 2007, **46**, 2152–2187.
- C. Dou, L. Han, S. Zhao, H. Zhang and Y. Wang, *J. Phys. Chem. Lett.*, 2011, **2**, 666–670.
- A. Julià-López, J. Hernando, D. Ruiz-Molina, P. González-Monje, J. Sedó and C. Roscini, *Angew. Chem.*, 2016, **128**, 15268–15272.
- Y. Wang, E. L. Runnerstrom and D. J. Milliron, *Annu. Rev. Chem. Biomol. Eng.*, 2016, **7**, 283–304.
- S. Han, J. Zhang, B. Teng, C. Ji, W. Zhang, Z. Sun and J. Luo, *J. Mater. Chem. C*, 2017, **5**, 8509–8515.
- Y. Hu, H. Zhang, W. K. Chong, Y. Li, Y. Ke, R. Ganguly, S. A. Morris, L. You, T. Yu, T. C. Sum, Y. Long and H. J. Fan, *J. Phys. Chem. A*, 2018, **122**, 6416–6423.
- P. Gütllich and H. A. Goodwin, Spin Crossover in Transition Metal Compounds II, in *Topics of Current Chemistry*, Springer, 2004, vol. 234.
- A. Bousseksou, G. Molnár, L. Salmon and W. Nicolazzi, *Chem. Soc. Rev.*, 2011, **40**, 3313–3335.
- W. Zhang, H.-Y. Ye, R. Graf, H. W. Spiess, Y.-F. Yao, R.-Q. Zhu and R.-G. Xiong, *J. Am. Chem. Soc.*, 2013, **135**, 5230–5233.
- C. Shi, X.-B. Han and W. Zhang, *Coord. Chem. Rev.*, 2019, **378**, 561.
- X.-H. Zhao, X.-C. Huang, S.-L. Zhang, D. Shao, H.-Y. Wei and X.-Y. Wang, *J. Am. Chem. Soc.*, 2013, **135**, 16006–16009.
- Y.-H. Luo, C. Chen, D.-L. Hong, X.-T. He, J.-W. Wang and B.-W. Sun, *J. Phys. Chem. Lett.*, 2018, **9**, 2158–2163.
- B. Sapparov and D. B. Mitzi, *Chem. Rev.*, 2016, **116**, 4558–4596.
- B. Kundys, a. Lappas, M. Viret, V. Kapustianyk, V. Rudyk, S. Semak, C. Simon and I. Bakaimi, *Phys. Rev. B: Condens. Matter Mater. Phys.*, 2010, **81**.
- Y. Zhang, W.-Q. Liao, D.-W. Fu, H.-Y. Ye, C.-M. Liu, Z.-N. Chen and R.-G. Xiong, *Adv. Mater.*, 2015, **27**, 3942–3946.
- H.-Y. Zhang, G.-Q. Mei and W.-Q. Liao, *Cryst. Growth Des.*, 2016, **16**, 6105–6110.
- M. A. Asghar, S. Zhang, T. Khan, Z. Sun, A. Zeb, C. Ji, L. Li, S. Zhao and J. Luo, *J. Mater. Chem. C*, 2016, **4**, 7537–7540.
- W. Zhang, H.-Y. Ye, H.-L. Cai, J.-Z. Ge, R.-G. Xiong and S. D. Huang, *J. Am. Chem. Soc.*, 2010, **132**, 7300–7302.

- 24 A. Sen, S. Roy, S. C. Peter, A. Paul, U. V. Waghmare and A. Sundaresan, *J. Solid State Chem.*, 2018, **258**, 431–440.
- 25 H.-Y. Ye, Y.-Y. Tang, P.-F. Li, W.-Q. Liao, J.-X. Gao, X.-N. Hua, H. Cai, P.-P. Shi, Y.-M. You and R.-G. Xiong, *Science*, 2018, **361**, 151–155.
- 26 W.-Q. Liao, Y. Zhang, C.-L. Hu, J.-G. Mao, H.-Y. Ye, P.-F. Li, S. D. Huang and R.-G. Xiong, *Nat. Commun.*, 2015, **6**.
- 27 Q. Guo, W.-Y. Zhang, C. Chen, Q. Ye and D.-W. Fu, *J. Mater. Chem. C*, 2017, **5**, 5458–5464.
- 28 W.-Q. Liao, Y.-Y. Tang, P.-F. Li, Y.-M. You and R.-G. Xiong, *J. Am. Chem. Soc.*, 2017, **139**, 18071–18077.
- 29 Y.-M. You, W.-Q. Liao, D. Zhao, H.-Y. Ye, Y. Zhang, Q. Zhou, X. Niu, J. Wang, P.-F. Li, D.-W. Fu, Z. Wang, S. Gao, K. Yang, J.-M. Liu, J. Li, Y. Yan and R.-G. Xiong, *Science*, 2017, **357**, 306–309.
- 30 C. S. Vogelsberg and M. A. Garcia-Garibay, *Chem. Soc. Rev.*, 2012, **41**, 1892–1910.
- 31 CrysAlisPro, Version 1.171.37.31, Agilent Technologies, Yarnton, UK, 2014, release 14.01.2014 CrysAlis171.NET.
- 32 G. M. Sheldrick, *Acta Crystallogr., Sect. A*, 2015, **71**, 3–8.
- 33 G. M. Sheldrick, *SHELXS97 Program for the Solution of Crystal Structures*, University of Göttingen, Göttingen, Germany, 1997.
- 34 L. Farrugia, *J. Appl. Crystallogr.*, 1999, **32**, 837–838.
- 35 P. E. Mason, G. W. Neilson, J. E. Enderby, M.-L. Saboungi, C. E. Dempsey, A. D. MacKerell and J. W. Brady, *J. Am. Chem. Soc.*, 2004, **126**, 11462–11470.
- 36 A. Kubičková, T. Křížek, P. Coufal, E. Wernersson, J. Heyda and P. Jungwirth, *J. Phys. Chem. Lett.*, 2011, **2**, 1387–1389.
- 37 M. Vazdar, F. Uhlig and P. Jungwirth, *J. Phys. Chem. Lett.*, 2012, **3**, 2021–2024.
- 38 D.-L. Hong, Y.-H. Luo, X.-T. He, C. Wang, J.-Y. Wang, F.-H. Chen, H.-S. Wu, C. Chen and B.-W. Sun, *ACS Appl. Mater. Interfaces*, 2019, **11**, 7272.
- 39 A. Gobbi and G. Frenking, *J. Am. Chem. Soc.*, 1993, **115**, 2362–2372.
- 40 D. A. Dougherty, *Science*, 1996, **271**, 163–168.
- 41 L. E. Orgel, *J. Chem. Phys.*, 1955, **23**, 1958.
- 42 L. E. Orgel, *J. Chem. Phys.*, 1955, **23**, 1824–1826.
- 43 K. E. Lawson, *J. Chem. Phys.*, 1967, **47**, 3627–3633.
- 44 H.-Y. Ye, Q. Zhou, X. Niu, W.-Q. Liao, D.-W. Fu, Y. Zhang, Y.-M. You, J. Wang, Z.-N. Chen and R.-G. Xiong, *J. Am. Chem. Soc.*, 2015, **137**, 13148–13154.
- 45 Y. Zhang, W.-Q. Liao, D.-W. Fu, H.-Y. Ye, Z.-N. Chen and R.-G. Xiong, *J. Am. Chem. Soc.*, 2015, **137**, 4928–4931.